PHOTONICS Research

Photon-counting optical time-domain reflectometry with centimeter-level spatial resolution over fibers of 100 km

XIZI SUN,[1] XIAOSONG REN,[2] ZHANPING JIN,[2] ZHISHENG YANG,[3] YIDONG HUANG,[1] AND WEI ZHANG[1,2,*]

[1]Beijing Academy of Quantum Information Sciences, Beijing 100193, China
[2]Frontier Science Center for Quantum Information, State Key Laboratory of Low-Dimensional Quantum Physics, Department of Electronic Engineering, Tsinghua University, Beijing 100084, China
[3]State Key Laboratory of Information Photonics & Optical Communications, Beijing University of Posts and Telecommunications, Beijing 100876, China
*Corresponding author: zwei@mail.tsinghua.edu.cn

Received 16 November 2025; revised 19 February 2026; accepted 26 February 2026; posted 26 February 2026 (Doc. ID 584953); published 28 April 2026

In this work, an experimental system is established to investigate the spatial resolution and signal-to-noise ratio (SNR) of photon-counting optical time-domain reflectometry (PC-OTDR) comprehensively. We analyze the impact of fiber dispersion on the spatial resolution, showing that light pulses at the C-band with a temporal width of several hundred picoseconds can support a spatial resolution of several centimeters over single-mode fibers (SMFs) of 100 km. We analyze the noises in the PC-OTDR measurement and calculate the SNRs along the OTDR traces under different conditions. These results show that the coherent Rayleigh noise (CRN) is the dominate noise, and it can be reduced by using a sampling bin width longer than the light pulse width. The experimental system is optimized accordingly, achieving a PC-OTDR experiment with a spatial resolution of 10 cm and a sensing range of 100 km. This shows that PC-OTDRs have strong capacity for long-distance high-resolution distributed sensing, which has great potential on optical link management and remote sensing over long-distance underground/submarine fiber cables.

https://doi.org/10.1364/PRJ.584953

1. INTRODUCTION

Distributed optical fiber sensing based on optical time-domain reflectometry (OTDR) offers the capability to obtain the spatial information of light propagation along optical fibers, which has been widely used in optical cable monitoring and management [1–3]. In an OTDR system, a light pulse is launched into the fiber under test, then the intensity variation of the Rayleigh backscattering light is measured with time, and the profile of transmission loss distribution and the location of abnormal events are obtained according to the light velocity in optical fibers [4]. Usually, linear detectors, such as PIN photodiodes or avalanche photodiodes (APDs), are used in OTDR systems [5]. To achieve a high spatial resolution, which refers to the ability to distinguish two closely spaced events along optical fibers, a wide detection bandwidth is preferred in OTDR systems using very short light pulses. On the other hand, the detection noise would rise under an increasing detection bandwidth, which decreases the detection sensitivity and reduce the sensing range of OTDR systems. Consequently, it is difficult for conventional OTDR systems to achieve high spatial resolution and long sensing range simultaneously.

In recent years, the technology of single-photon detection in telecom band developed rapidly and has been widely used in quantum communications and photonic quantum information processing [6–9]. As an advanced light detection method, it is also applied in applications of optical sensing such as photon-counting OTDR (PC-OTDR) [10–14]. PC-OTDR combines the characteristics of single-photon detectors (SPDs) and time-correlated single photon counting (TCSPC) technology. The single-photon-level sensitivity of SPDs enables the detection of ultra-weak backscattering lights when very short light pulses propagate along optical fibers, which is required to achieve high spatial resolution in OTDR measurement. Besides, the time jitter of SPDs and TCSPC measurement is quite low, indicating that it is possible to achieve a high spatial resolution of several centimeters in PC-OTDR. Hence, PC-OTDR does not have the limitation of conventional OTDR to realize high spatial resolution measurements over long sensing ranges. Researchers have reported spatial resolution below/at the centimeter scale.

For example, Zhao *et al.* obtained a spatial resolution of 4 mm by a PC-OTDR system using superconducting nanowire single-photon detectors (SNSPDs) [15]. Hu *et al.* demonstrated a spatial resolution of 6.0 cm over a piece of standard single-mode fiber of 2.0 km [16]. Calliari *et al.* realized 4.6 cm spatial resolution monitoring of 12 km fiber within 20 min [17], and Legré *et al.* achieved a spatial resolution of 5.1 cm with 50 km sensing range, which, to the best of our knowledge, is the longest experimental result under such a high spatial resolution [18]. To further enhance the performance of high-spatial-resolution PC-OTDR, several key optimization directions should be clarified. What are the characteristics of the pulsed light source used in this system? How does the fiber dispersion affect the spatial resolution? How could the signal-to-noise ratio (SNR) of this system be analyzed accurately? A comprehensive theoretical and experimental investigation into the physical processes of PC-OTDR is essential.

In this work, we established a PC-OTDR system to explore how to achieve long sensing range and high spatial resolution simultaneously. First, the light pulses in this system are optimized to achieve high spatial resolution and long sensing range simultaneously, considering both the fiber dispersion and the time jitter of the single-photon detection in the system. Then, we analyze the SNR of this system considering all the noises in the system, including the dark counts of the SPD, the photon counting fluctuation due to the Poisson distribution, and the coherent Rayleigh noise (CRN). Finally, according to the analysis in previous sections, the system is optimized, and we achieve a PC-OTDR experiment with a spatial resolution of 10 cm and a sensing range of 100 km. In addition, the spatial resolution of 10 cm is also verified over an 81.7 km fiber link, including deployed fibers of 30.9 km. This shows that PC-OTDR has strong capacity for long-distance high-resolution distributed sensing.

2. THE PC-OTDR SYSTEM

As shown in Fig. 1(a), we establish an experimental system to investigate the physical processes in PC-OTDR. It is designed to achieve high spatial resolution over single-mode fibers (SMFs) using light pulses near 1550 nm. Considering the impact of fiber dispersion on the spatial resolution, narrowband light pulses without chirp are preferred. A pulsed semiconductor laser is used as the light source, generating light pulse series at 1550.12 nm. The width of the generated light pulses can be adjusted from 50 ps to 2 ns by controlling the electrical driving signal. A narrowband optical filter is used to remove the large chirp at the beginning of the pulses. The light source is triggered by a digital delay generator (SRS, DG645), and the period of the light pulse series is 1.1 ms, which can support an OTDR measurement over silica optical fibers of 110 km. The light pulses are amplified by an erbium-doped fiber amplifier (EDFA), and then pass through an optical filter to remove the amplified spontaneous emission (ASE) of the EDFA. A variable optical attenuator (VOA) is used to adjust the intensity of the light pulses, ensuring that the SPD would not be saturated by the backscattering light from the optical fibers. The light pulses are launched into the fiber under test (FUT) through a circulator (Port 1 to Port 2). When the light pulses propagate along the FUT, the backward light is generated due to the Rayleigh backscattering and discrete reflection points and output from the FUT through the same circulator (Port 2 to Port 3). Then, it is detected by a superconducting nanowire single-photon detector (SNSPD, Photec Inc., P-SPD-8S), which operates in the free-running mode, with a detection efficiency of 90% and a dark counting rate (DCR) of 100 Hz. The electric signal output from the SNSPD is recorded by the equipment of TCSPC (Swabian, Time Tagger Ultra), which operates in histogram mode with the specified time bin width and measurement time. The TCSPC is triggered by a periodic electrical signal that is generated by the digital delay generator and that synchronizes with the trigger signal of the pulsed light source. Hence, the time delay of each detected photon with respect to the launch time of the laser pulse is recorded by the TCSPC. The distance between the input end of the FUT and the location at which the backward photon is generated can be calculated by $z = c\Delta t/2n_{\mathrm{eff}}$, where c is the light velocity in a vacuum, n_{eff} is the effective refractive index of the silica fibers, and Δt is the measured time delay. The OTDR trace is reconstructed by making a histogram of these recorded single photon events as a function of the location along the FUT.

In the system shown in Fig. 1(a), the maximum counting rate of the SNSPD (~8 MHz) limits the intensity of the light pulse series; hence, it also limits the sensing range. To extend the sensing range of this system, the external gate control [19] on the single-photon detection is applied by an acousto-optic modulator (AOM) for long-distance OTDR experiment (see Section 5), as shown in Fig. 1(b). The driving signal of the AOM is also generated by the digital delay generator and synchronizes with the light pulses. The AOM provides a detection window with a specific time delay to the light pulse in each period. Proper attenuation is applied on the light pulses by the VOA to ensure that the backward photons would not saturate the SNSPD in this detection window. The whole OTDR trace can be reconstructed by the measurement results under the detection windows with different time delays.

3. THE LIGHT SOURCE OPTIMIZATION OF THE PC-OTDR WITH HIGH SPATIAL RESOLUTION

Considering that there is a discrete reflection point in the FUT, the light pulses are reflected by it, generating the

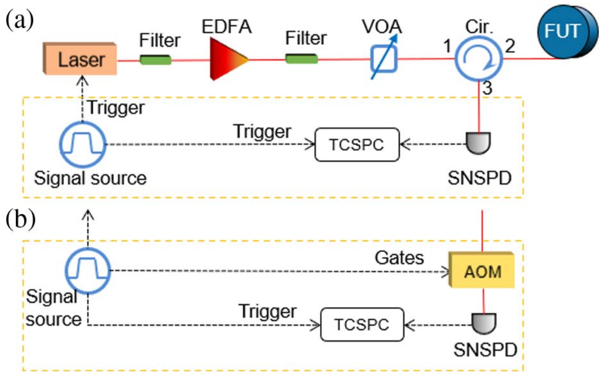

Fig. 1. Sketch of the PC-OTDR system (a) without and (b) with the external gate control on the single-photon detection.

backward photons. The single-photon detection events of these photons would accumulate on the histogram, forming a peak on the OTDR trace. If the FUT has two discrete reflect points with a space smaller than the width of the peak, the backward photons reflected by the two points could not be discriminated. Hence, the spatial resolution of the PC-OTDR system can be indicated by the width of the peak on the OTDR trace. The spatial resolution, which is denoted by S, is determined by two physical factors: the time jitter of the TCSPC measurement and the wavepacket width of the backward photons reflected by a discrete point in the fiber [17,20].

The time jitter of the TCSPC measurement, which is denoted by $\Delta\tau$, includes the contributions of the SPD, the TCSPC equipment, the electrical delay generator, the opto-electrical process in the laser source, and so on. It can be calculated by the time jitters of these equipment and devices shown in the specifications or measured experimentally. It is worth noting that the commercial SPDs at the telecom band usually have time jitters over 100 ps, much larger than other contributions, and dominate the time jitter of the TCSPC measurement. The time jitter $\Delta\tau$ provides an upper bound of the spatial resolution of the PC-OTDR system.

The other factor is due to the physical process when the light pulses propagate along the optical fibers. For the backward photons reflected by a discrete reflection point, the width of the wavepackets of these photons is determined by the initial width of the light pulses and the effect of the fiber dispersion. If the optical fibers have large dispersion at the wavelength of the light pulses, as the PC-OTDR system shown in Section 2, the pulse broadening due to the fiber dispersion would seriously impact the spatial resolution. Hence, light pulses with narrow linewidth are preferred to reduce the impact of fiber dispersion. For simplicity in the following analysis, the Gaussian light pulses with Fourier-transform-limited pulse widths are considered. The Gaussian profile of the light pulses and the single-photon wavepackets of the backward photons maintains when they propagate along the fibers, while the width of these pulses increases with the propagating length. Considering that a backward photon is generated by scattering or reflection at a specific location in the FUT, and the distance between this location and the input end of the FUT is z, the wavepacket width of this photon when it is output from the FUT can be expressed as [21]

$$T_{\text{pulse}} = T\sqrt{1 + (2z|\beta_2|/T_0^2)^2}, \tag{1}$$

where T_{pulse} and T are the temporal full-widths at half-maximum (FWHMs) of the wavepacket output from the FUT and the light pulse when it is launched into the FUT, respectively. β_2 is the group velocity dispersion parameter of the FUT. T_0 is the half-width at $1/e$-intensity point of the light pulses, and $T = 2\sqrt{\ln 2}\,T_0$.

Considering both factors, the spatial resolution of the PC-OTDR system can be expressed as

$$S = \frac{c}{2n_{\text{eff}}}\sqrt{T_{\text{pulse}}^2 + \Delta\tau^2}, \tag{2}$$

where c is the light velocity in a vacuum, and n_{eff} is the effective refractive index of the FUT. According to Eq. (2), the spatial resolutions of the PC-OTDR system shown in Section 2 are calculated, and the results are shown in Fig. 2(a). In the calculation, the FUT is SMFs of 100 km, and its group velocity dispersion parameter and effective refractive index at 1550 nm are 20 ps^2/km and 1.46, respectively. The time jitter of the TCSPC measurement $\Delta\tau$ is 118 ps, corresponding to a spatial resolution of 1.21 cm, which is calculated by the time jitters of the SNSPD and other electrical equipment. Several FWHMs of the input light pulses are considered in the calculation, covering the scenarios with centimeter-level spatial resolution. Their results are indicated by the curves with different colors. It can be seen that all the curves rise with increasing distance, and the highest resolution appears near the input end of the FUT. If the width of the light pulses is smaller than $\Delta\tau$, such as $T = 25$ ps and 50 ps, the spatial resolution increases rapidly due to the fiber dispersion, and the highest resolution is mainly determined by $\Delta\tau$. When the width of the light pulses is comparable with $\Delta\tau$ ($T = 100$ ps), the spatial resolution shows slower increase under increasing distance due to its narrower linewidth, and the pulse width contributes to the highest resolution obviously. In the cases that the widths of the light pulses are far larger than $\Delta\tau$ ($T = 200$ ps, 300 ps, and 400 ps), it can be seen that the spatial resolutions are almost unchanged since the effect of fiber dispersion is quite small for these light pulses during the FUT of 100 km. The spatial resolution is mainly determined by the pulse widths. Hence, to achieve a high spatial resolution over the FUT of 100 km, the width of the light pulses should be large enough to avoid the impact of fiber dispersion. On the other hand, it could not be too large to satisfy a specific resolution requirement. For the requirement of centimeter-level resolution, the pulse width of several hundred picoseconds is acceptable.

To demonstrate the above analysis, the OTDR traces of the system shown in Section 2 are measured under different pulse widths. The FUT in these measurements consist of five fiber spools of 20 km SMFs, connected to each other by FC/UPC-connectors. The OTDR trace measured using light pulses with a width of 300 ps is shown in Fig. 2(b). It can be seen that several peaks appear on the trace, which are due to the discrete Fresnel reflections at the joint points of two fiber spools by the connectors. The inset shows the normalized profiles of each peak, and the widths of these peaks show the spatial resolutions at the corresponding locations along the FUT. Figure 2(c) shows the measurement results of the spatial resolution of the PC-OTDR system along the FUT under different pulse widths. It can be seen that the measurement results agree well with the theoretical calculations shown in Fig. 2(a).

Figure 2 shows the results of the PC-OTDR system with the pulsed light source at 1550 nm and the FUT of SMFs for long-distance applications. It is worth noting that a similar analysis could be applied on other PC-OTDR systems and different results of the light source optimization could be obtained. For example, if the system uses a pulsed light source near 1310 nm, which is close to the zero dispersion point of SMF, it can be expected that the impact of fiber dispersion could be neglected, and the spatial resolution would be unchanged along the fiber and fully determined by the input pulse width and the time jitter of the TCSPC measurement.

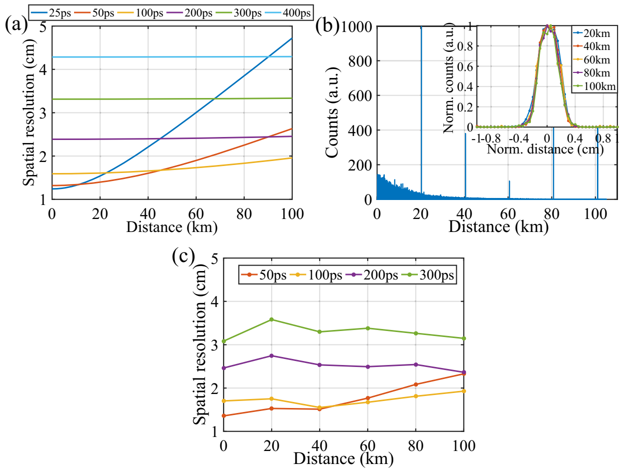

Fig. 2. Theoretical and experimental results of the spatial resolutions of the PC-OTDR system under different pulse widths. (a) Calculation results, (b) the OTDR trace measured using light pulses with a width of 300 ps and the normalized profile of each reflection peak, (c) the measured spatial resolutions along the FUT.

If a pulsed light source near 1625 nm is used, which is one of the common wavelengths employed in commercial OTDR, a larger impact of fiber dispersion could be expected in SMFs. A wider pulse width would be preferred comparing with the case shown in Fig. 2.

4. NOISE ANALYSIS OF THE PC-OTDR WITH HIGH SPATIAL RESOLUTION

As shown in the OTDR trace in Fig. 2(b), a clear noise distribution along the fiber can be observed, which almost impedes the extraction of the backscattered Rayleigh signal. In this section, different noise contributions in the PC-OTDR system are analyzed by theoretical analysis and experiments, and the measures to suppress the noises are discussed.

The noise model is established under the condition that the extinction ratio of the optical pulse is infinite, excluding intraband noise caused by the continuous wave. In a PC-OTDR system, the detection noise is essentially due to the dark counts of the SPD and the fluctuation by the Poisson statistics of photon counting [22]. Their contributions to the fluctuation variances of the single photon detection events can be expressed as

$$\text{Dark noise}:\ \sigma_{\text{dark}}^2 = R_{\text{dark}} t_{\text{bin}} N, \tag{3}$$

$$\text{Fluctuating noise}:\ \sigma_{\text{fl}}^2 = R(z) t_{\text{bin}} N, \tag{4}$$

where R_{dark} is the DCR of SPD, which is constant for a specified SPD and can be obtained experimentally. $R(z) = \frac{\eta \alpha_{\text{ray}} c T P_p e^{-2\alpha z}}{2 n_{\text{eff}} h\nu}$, which is the count rate of Rayleigh backscattering photons. Parameters η, α_{ray}, α, P_p, h, and ν are the detection efficiency of the SPD, Rayleigh scattering coefficient, attenuation coefficient of the optical fiber, peak power of the pulse at fiber input, Planck constant, and laser frequency, respectively. t_{bin} denotes the bin width in the measurement, which corresponds to the sampling interval. $N = t_{\text{meas}}/t_{\text{period}}$, which represents the number of light pulses in the measurement. Here, t_{meas} and t_{period} are the measurement time and the period of the pulse series, respectively.

As with the analysis in the last section, the light pulses with a width larger than 100 ps should be selected for the PC-OTDR system with a centimeter-level spatial resolution. The larger the pulse width, the narrower its spectral width, and consequently, the longer its coherence length. Rayleigh scattering light within the coherent length interferes with each other and forms a random noise, named CRN. The intensity of CRN depends on the intensity of the backscattered light and the phase difference within the coherent length [5]. For a Fourier-transform-limited Gaussian light pulse, the coherence length could be estimated by its pulse width. For a pulse with a sub-nanosecond width, the coherence length is shorter than 20 cm in the silica optical fibers. The intensity of the backscattered light is almost unchanged within such a short fiber length. Additionally, the phase differences are randomly distributed along the fiber. The standard deviation (STD) of CRN is proportional to the Rayleigh scattering intensity in this case and can be expressed as (for the derivation see the Appendix B)

$$\sigma_{\text{CRN}} = K R(z) t_{\text{bin}} N \qquad t_{\text{bin}} \le T, \tag{5a}$$

$$\sigma_{\text{CRN}} = K R(z) N \sqrt{2T t_{\text{bin}} - T^2} \qquad t_{\text{bin}} > T, \tag{5b}$$

where K is a scaling factor of this proportional relation, which relates to the characteristics of the light source and the FUT and can be estimated according to the experimental data. Combining Eqs. (3)–(5), the STD of the total noise can be written as

$$\sigma_{\text{total}} = \sqrt{\sigma_{\text{dark}}^2 + \sigma_{\text{fl}}^2 + \sigma_{\text{CRN}}^2}. \tag{6}$$

An experiment of PC-OTDR over a 50 km SMF is carried out using the setup shown in Fig. 1(a) to indicate the impacts of the three noise contributions. First, the scenario under $t_{\text{bin}} \le T$ is considered. The OTDR traces are measured under the light pulse widths (T) of 300 ps and 1 ns, respectively. The width of the time bin (t_{bin}) is 100 ps, the number of the light pulses (N) is 1.5×10^7, and the light pulse intensities are controlled carefully to ensure that $R(0) = 2$ MHz in these measurements. The noise STDs (blue curves) of the traces along the FUT are calculated based on every 20 adjacent sampling counts and are shown in Figs. 3(a) and 3(b), respectively. Additionally, the STDs of the total noise and the three noise contributions are calculated according to Eqs. (3)–(6), plotted as the curves with different colors in these figures. In the calculation of Eq. 5(a), $K = 0.7$ is used to fit the calculated total noise STDs to the experiment results. It can be seen that the calculated total noise STDs agree well with the experiment results in both figures. The results of different light pulse widths shown in these two figures are almost the same, indicating that the noise is mainly determined by the detected photon count rate. To show it more clearly, we also measure the OTDR traces under $R(0) = 1$ MHz when the widths of the light pulses are 300 ps and 1 ns, respectively. The results are plotted in Figs. 3(c) and 3(d), showing that the noise STDs along the traces have the same profiles as those in Figs. 3(a) and (b),

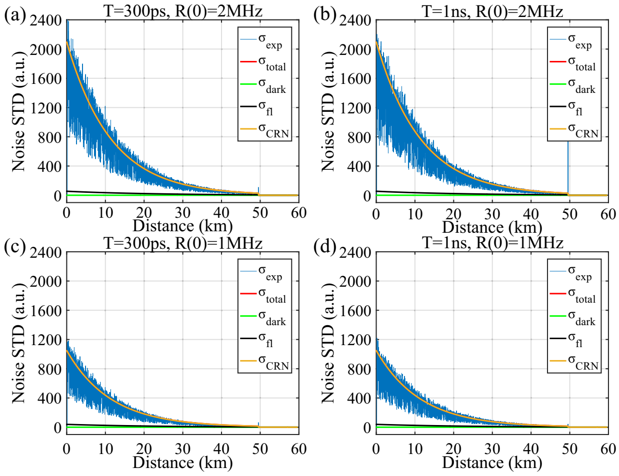

Fig. 3. Noise STDs over 50 km SMF for $R(0) = 2$ MHz when (a) $T = 300$ ps and (b) $T = 1$ ns and for $R(0) = 1$ MHz when (c) $T = 300$ ps and (d) $T = 1$ ns. Relevant parameters are $t_{\mathrm{bin}} = 100$ ps, $N = 1.5 \times 10^7$.

but the values are a half of them. In all the panels of Fig. 3, the total noise STDs decrease along the traces. At the near-end of the FUT, the CRN dominates the total noise. However, the CRN decreases more rapidly than other noise contributions. It can be expected that if the FUT is long enough, the contribution of the CRN would be comparable with the other two at the far-end of the FUT.

To reduce the CRN, a longer sampling width leading that t_{bin} is much higher than T and is preferred since the fluctuation introduced by the CRN can be reduced by averaging the photon counts in a wider time bin width larger than the coherence length according to Eq. (5). The similar experiments are carried out to show the effect of averaging under the condition that $T = 300$ ps, $R(0) = 1$ MHz, and $t_{\mathrm{bin}}N = 1.5 \times 10^{-3}$ [keeping the same photon count as results of Fig. 4(c)]. The OTDR traces are measured under $t_{\mathrm{bin}} = 1$ ns, 2 ns, and 5 ns, and the results are shown in Figs. 4(a)–4(c), respectively. It is worth noting that N is adjusted in each calculation to ensure that the photon count is consistent; hence, the noise STDs are compared under the same signal level [i.e., $R(z)t_{\mathrm{bin}}N$]. The CRN STD as a function of fiber distance is calculated based on Eq. (5b) under $k = 0.7$, as shown in the yellow curves in Fig. 4. The total noise STDs described by Eqs. (3)–(6) match well with the measured results in all cases, demonstrating the correctness of these equations. Comparing the results of Figs. 3(c) and 4 shows that CRN can be suppressed effectively by increasing t_{bin}. It also shows that for long-range sensing, the impact of CRN highly reduces at the far end of the FUT where the detected photon count is low, and it may be comparable to, or even lower than the fluctuation due to other noise contributions, as shown in the insets in Figs. 4(a)–4(c).

The SNR of the PC-OTDR is defined by the ratio of the averaged detected photon counts per time bin and the noise STD [23] and can be expressed by $\mathrm{SNR} = R(z)t_{\mathrm{bin}}N/\sigma_{\mathrm{total}}$. The three panels in Fig. 5 show the calculated SNRs under increasing fiber distance when $R(0) = 1$ MHz, $t_{\mathrm{bin}}N = 1.5 \times 10^{-3}$, and $T = 100$ ps, 200 ps, and 300 ps, respectively.

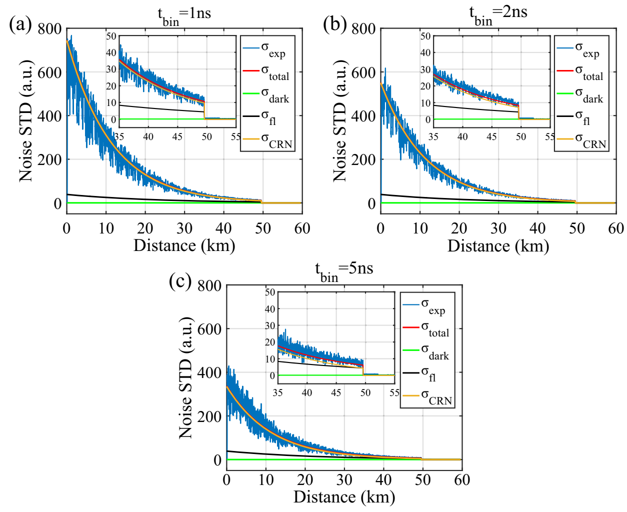

Fig. 4. Noise STD over 50 km SMF for (a) $t_{\mathrm{bin}} = 1$ ns, (b) $t_{\mathrm{bin}} = 2$ ns, and (c) $t_{\mathrm{bin}} = 5$ ns. Relevant parameters are $T = 300$ ps, $R(0) = 1$ MHz, and N is adjusted in each measurement to make $t_{\mathrm{bin}}N = 1.5 \times 10^{-3}$.

The results with different time bin widths (t_{bin}) are indicated by the curves with different colors. If $t_{\mathrm{bin}} \le T$, the SNR remains 1.5 dB and unchanged along the FUT [the blue curves in Figs. 5(a)–5(c) and the orange curve in Fig. 5(c)]. In these cases, the CRN is the dominate noise. It is proportional to the Rayleigh scattering intensity, as shown in Eq. (5a), leading to a constant SNR along the OTDR trace. When t_{bin} is larger than T, the SNR is enhanced since a larger t_{bin} is preferred to suppress the CRN. Moreover, a shorter pulse width is also helpful to achieve a higher SNR. It can be seen that the pulse width T and the time bin width t_{bin} jointly determine the SNR and the spatial resolution. They should be optimized carefully to achieve a high spatial resolution over a long sensing range, as demonstrated by the experiment shown in Section 5. In addition, the CRN reduces faster than other noise contributions under increasing distance. At the far end of the FUT, the fluctuating noise might be dominant, and this leads to the SNR showing a proportionality to fiber attenuation.

5. PC-OTDR EXPERIMENT WITH 10 cm SPATIAL RESOLUTION OVER OPTICAL FIBERS OF 100 km AND DEPLOYED FIBER

The long-distance PC-OTDR with a spatial resolution of 10 cm over optical fibers of 100 km is achieved using the PC-OTDR system with the external gate control shown in Fig. 1(b). The light pulse width and time bin width are set to $T = 100$ ps and $t_{\mathrm{bin}} = 500$ ps in the experiment, respectively, to achieve an SNR exceeding 3 dB, which is indicated in the calculation result shown in Fig. 5(a). In this system, the time bin width is longer than the theoretical spatial resolution determined by the pulse width and the time jitter of the TCSPC measurement [see Eq. (2)]. Hence, its spatial resolution is mainly determined by the time bin width and could be estimated by $S = ct_{\mathrm{bin}}/n_{\mathrm{eff}}$ according to the Nyquist sampling

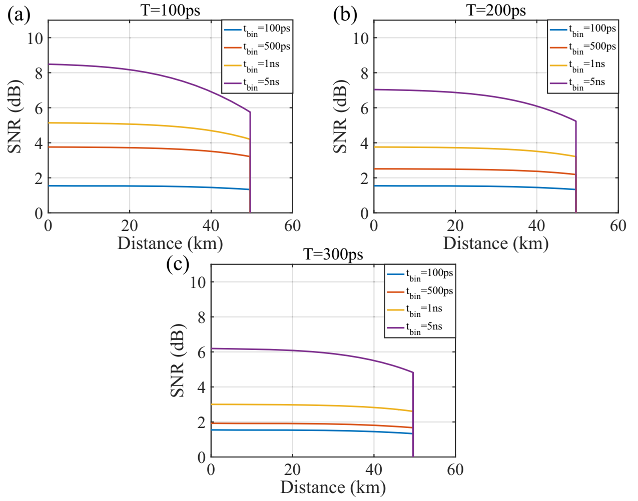

Fig. 5. SNR over 50 km SMF for (a) $T = 100$ ps, (b) $T = 200$ ps, and (c) $T = 300$ ps under sampling bin widths $t_{\mathrm{bin}} = 100$ ps, 500 ps, 1 ns, and 5 ns. In the calculations, $R(0) = 1$ MHz, and N is adjusted to make $t_{\mathrm{bin}}N = 1.5 \times 10^{-3}$.

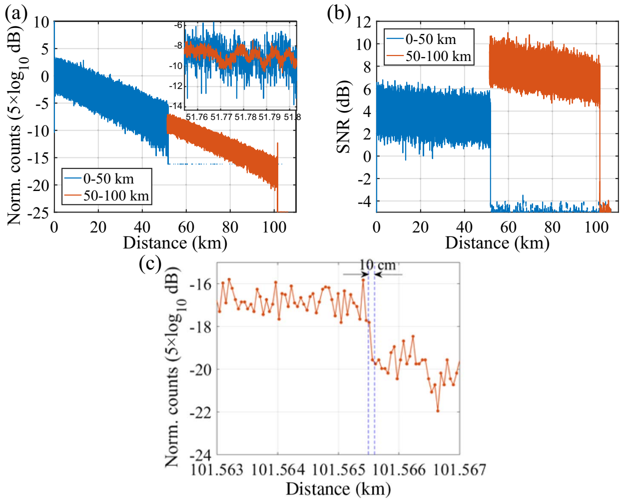

Fig. 6. Experiment results of the PC-OTDR with high spatial resolution over optical fibers of 100 km. (a) The OTDR traces in logarithmic scale, (b) the SNR over the FUT, and (c) the OTDR trace over a fiber section from 101.563 km to 101.567 km.

theorem [23]. Accordingly, a spatial resolution of 10 cm over optical fibers of 100 km could be expected in this system.

The external gate control is used to overcome the limitation of sensing range due to the maximum counting rate of the SNSPD [19]. The width of the gating window is set to be 510 μs. By controlling the delay of the gating signal, the OTDR trace of the FUT of 101.8 km is acquired through two measurements. In the first measurement, the gate is set to measure the optical fibers of 50.9 km at the near end of the FUT. In this measurement, the intensity of the light pulses is controlled to ensure that the maximum counting rate of the backscattered photons is close to the saturation limit of the SNSPD. In the second measurement, the gate is set to measure the optical fibers of 50.9 km at the far end of the FUT. The intensity of the light pulses is increased to achieve the same maximum counting rate of the backscattered photons. Since both the light pulses and the backscattered photons experience the transmission loss of the near-end fiber of 50.9 km, it can be expected that the intensity of the light pulses should be improved by 19.3 dB (the attenuation coefficient of the FUT is 0.19 dB/km) compared with that in the measurement for the near-end fiber. In each measurement, the time of the single photon detection is 10 min, leading to a total measurement time of 20 min.

The acquired OTDR trace is shown in Fig. 6(a), where the blue and red curves are the results of the near-end fiber and far-end fiber, respectively. They are combined sequentially based on (1) the time delay of the gating signals and (2) amplitude processing to ensure that both traces are matched in the region near the distance of 51 km where they overlap, as shown in the inset of Fig. 6(a). The SNR along the OTDR trace is calculated and shown in Fig. 6(b). It can be seen that the SNR of the near-end fiber of 50.9 km remains ∼3.5 dB under increasing distance, in agreement with the calculation result shown by the yellow curve in Fig. 5(a). On the other hand, the SNR of the far-end fiber of 50.9 km is obviously higher than that of the near-end fiber. It is due to the large intensity difference of the light pulses in the two measurements. The high intensity of the light pulses in the second measurement would lead to nonlinear effects such as modulation instability and four-wave mixing [21,24], which would induce spectral broadening and reduce the coherence of the light pulses. Consequently, it would lead to suppression of the CRN and improvement of the SNR (details are elaborated in Appendix A).

It can be expected that the spatial resolution would worsen along the OTDR trace in this PC-OTDR system. Hence, an abrupt attenuation event is introduced at the end of the FUT to show the spatial resolution. The OTDR trace near the attenuation event is shown in Fig. 6(c). It can be seen that the length of falling edge that indicates the spatial resolution is correctly detected, showing a spatial resolution of 10 cm.

Furthermore, the performance of the PC-OTDR system is demonstrated on an 81.7 km FUT with an SMF fiber spool of 50.8 km and a deployed fiber cable link of 30.9 km. As illustrated in Fig. 7(a), the deployed fiber is laid between the ROHM Building on the campus of Tsinghua University and the building of BAQIS. The PC-OTDR system and the SMF fiber spool are placed at the building of BAQIS. The experimental parameters are consistent with those used to acquire the curves in Fig. 6(a), with two modifications for the measurement of the near-end fiber of 50.8 km: (1) the pulse intensity is increased by 19.3 dB, and (2) a 19.3 dB fixed attenuator is inserted before the SNSPD to attenuate the highly backscattered Rayleigh light from the near-end fiber of 50.8 km to avoid the saturation of the SNSPD. The acquired OTDR trace is shown in Fig. 7(b), where the yellow and red curves correspond to the results of the near-end fiber of 50.8 km and the far-end deployed fiber of 30.9 km, respectively. As shown in the inset of Fig. 7(b), the overlapping regions of the two traces exhibit excellent agreement. Note that the SNR distribution along the fiber is non-uniform, which is primarily governed by the light pulse intensity (a detailed analysis is provided in Appendix A).

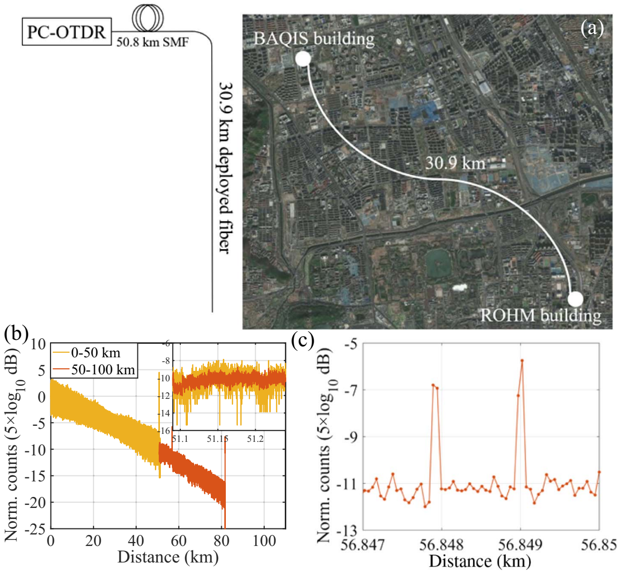

Fig. 7. Experimental results of the PC-OTDR with high spatial resolution over an 81.7 km FUT. The FUT comprises an SMF fiber spool of 50.8 km and a deployed fiber cable link of 30.9 km. (a) Top view of the deployed fiber topology at Haidian District, Beijing. (b) The OTDR traces in logarithmic scale. (c) The reflection peaks detected on the deployed fiber.

Several discrete peaks can be observed on the OTDR trace, originating from Fresnel reflections at the connector joints of fibers, which is common in the deployed fibers. Such fibers are typically connected by end-to-end splicing of underground pre-embedded fiber cables, leading to inevitable interface reflections. Figure 7(c) shows a magnified view of the OTDR trace over the deployed fiber segment, spanning 56.847 km to 56.85 km. Within this deployed fiber segment, two independent reflection peaks with an interval of 1 m are identified, and the FWHM of each reflection peak is 10 cm. This result directly confirms that the PC-OTDR system achieves a spatial resolution of 10 cm.

6. DISCUSSION

In the experiment shown in Section 5, the light pulse widths are 100 ps and the time jitter is 118 ps, which are both measured when the setup is under preparation. According to Eq. (2), a high spatial resolution of ~2 cm can be achieved. However, to mitigate the SNR deterioration caused by CRN, a time bin width of $t_{\mathrm{bin}} = 500$ ps is used in the experiment, which is far larger than the light pulse width and the time jitter, and it determines the spatial resolution of this PC-OTDR system. Additionally, a longer time bin width is also helpful to improve the photon counting number per time bin, which is preferred to reduce the measurement time (t_{meas}) under the same target SNR. Hence, the impacts of the time bin width on both the spatial resolution and the SNR should be considered in the PC-OTDR system. A reasonable way of the system design is that t_{bin} should be determined according to the spatial resolution requirement first, and then a proper N should be selected to achieve an acceptable SNR after a pulse width T much smaller than t_{bin} is determined.

According to the theoretical analysis in Section 4 and the experiment results in Section 5, the SNR of the OTDR trace is limited by the CRN. Previous research has shown that the CRN can be highly reduced by using a wideband light source [5]. However, it is not suitable for the high-resolution measurement since the temporal broadening of the wideband light pulses is serious due to the fiber dispersion and worsens the spatial resolution. The frequency shift averaging (FSAV) [25–27] is another method to reduce the CRN in the OTDR. It is implemented by tuning the frequency of the laser pulse to change the phase correlation between scattering points. As a result, the CRN can be effectively reduced by averaging many backscattering signals with different frequencies. However, the effect of fiber dispersion also should be considered in FSAV in the high spatial resolution measurement [28]. The range of frequency tuning would be limited to ensure the high spatial resolution, which limits the effect of the CRN suppression by the FSAV. It can be expected that the FUTs with low fiber dispersion at the wavelength of light pulses are preferred to achieve higher spatial resolution over long-distance optical fibers, such as the SMFs, if light pulses at the O-band are used, or the dispersion shifted fibers, if light pulses at the C-band are used. When the CRN is substantially suppressed, the total noise would be mainly dominated by the fluctuating noise.

According to the experiment, the sensing distance is mainly limited by the saturation of the SPD. By using the technique of the external gate control, the sensing distance is highly improved by dividing the FUT into two pieces and measuring them, respectively. In principle, the sensing distance could be further improved by enhancing the intensity of light pulses and splitting the FUT into more pieces. The last limitation would be the impact of a nonlinear effect in the optical fibers if the intensity of light pulses is too high. The temporal width variation or distortion of light pulses due to nonlinear effects such as self-phase modulation and fiber dispersion [21] would potentially cause the spatial resolution degradation and OTDR trace distortion.

It is worth noting that the simulation and experiment in this work are conducted based on the SNSPD featuring low dark noise. The analysis method also can be applied to the systems using other types of SPDs, such as Si-APD [18,28], Ge-APD [29], and InGaAs/InP-APD [22,30], considering the performance of different SPDs.

7. CONCLUSION

In this work, a PC-OTDR system is established to achieve high spatial resolution over long fiber distances. First, we analyze the impact of fiber dispersion on the spatial resolution based on the propagating and scattering process of Gaussian light pulses. This shows that light pulses at the C-band with a temporal width of several hundred picoseconds can support a spatial resolution of several centimeters over SMFs of 100 km. Then, we analyze the noises in the PC-OTDR measurement, including the dark counts of the SPD, the fluctuating noise due to the Poisson distribution, and the CRN. The SNR of the OTDR trace along the FUT can be estimated. This shows that the

CRN is the dominate noise, and it can be reduced by using a sampling bin width longer than the light pulse width. The experimental system is optimized according to above analysis, and the external gate control is applied to overcome the saturation of the SNSPD in the system. We achieve a PC-OTDR experiment with a spatial resolution of 10 cm and a sensing range of 100 km. Moreover, the 10 cm spatial resolution is also verified over an 81.7 km fiber link, including deployed fibers of 30.9 km. This shows that PC-OTDR has a strong capacity for long-distance high-resolution distributed sensing, which has great potential for optical link management and remote sensing over long-distance underground/submarine fiber cables.

APPENDIX A

In this appendix, we experimentally demonstrate and mathematical analyze the impact of pulse intensity on the noise, aiming to explain the mechanism for the SNR improvement in the long-range fiber sensing shown in Section 5. For the measurements shown in Fig. 6, in order to achieve the same maximum counting rate of the backscattered photons, the pulse intensity used in the second measurement (targeting the far-end 50.8 km) increases by 19.3 dB relative to that used in the first measurement (targeting the near-end 50.8 km), and the SNR of the far-end fiber of 50.8 km is much higher than that of the near-end fiber. It is worth noting that SNR improvement can be also observed when such high intensity of the light pulses is applied to the measurement of the near-end 50.8 km fiber. In this measurement (referred to as the third measurement hereafter), the system parameters remain consistent with those of the first measurement, with only two modifications implemented: (1) the pulse intensity is increased by 19.3 dB, and (2) a 19.3 dB fixed attenuator is inserted before the SNSPD to attenuate the highly backscattered Rayleigh light from the near-end 50.8 km fiber segment, thereby preventing detector saturation and ensuring that the maximum counting rate of the backscattered photons remains consistent with that of the first two measurements.

Figure 8(a) shows the acquired OTDR trace of the third measurement (yellow curve), overlaid with the traces from the first and second measurements [corresponding to the blue and red curves in Fig. 6(a), respectively] for comparative analysis. Note that the trace of the second measurement is plotted after the amplitude processing to ensure that all traces are matched in the region near the distance of 51 km where they overlap. In fact, the backscattered photons reaching the SNSPD remain consistent across the three measurements.

The noise STDs of these traces along the FUT are calculated based on every 20 adjacent sampling counts and are shown in Figs. 8(b). Additionally, for the first measurement, the STDs of the total noise and its individual components are calculated according to Eqs. (3)–(6) and plotted as the curves with different colors in Fig. 8(b). First, comparing the noise STDs of the first and third measurements, it can be observed that at the initial fiber position, CRN is the dominant noise, and the noise levels are consistent across traces obtained with different pulse powers. When low pulse intensity is applied, the STD of the CRN decays exponentially due to fiber loss. In contrast, under high pulse intensity, the STD of the CRN decreases more rapidly with distance. This is mainly because the high pulse intensity would lead to nonlinear effects such as modulation instability and four-wave mixing, which would induce spectral broadening and reduce the coherence of the light pulses, resulting in a suppression of the CRN. When the fiber length exceeds the effective nonlinear length (approximately 25 km in this case), the nonlinear effect is significantly attenuated by fiber loss, and its impact on CRN diminishes.

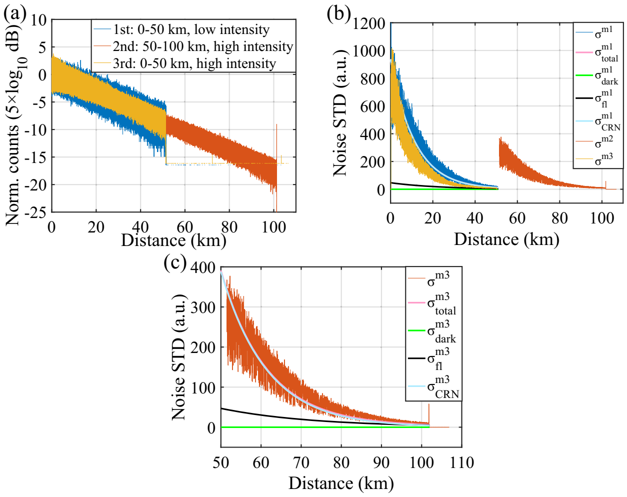

Fig. 8. (a) OTDR traces in the logarithmic scale of the three measurements. (b) The noise STDs of the three measurements and the theoretical profiles of the first measurement. (c) The experimental and theoretical noise STDs of the second measurement.

Then, comparing the noise STDs of the second and third measurements where both use the same high intensity of pulse light, the consistency in the nonlinear effect-induced CRN modulation leads to identical CRN evolution along the fiber. Based on the above analysis, the STD of total noise in the second measurement σ^{m_2} can be derived from the STD of noise in the third measurement σ^{m_3}, following these steps.

(1) Calculation of the STD of CRN in the third measurement $\sigma_{\mathrm{CRN}}^{m_3}$

The $\sigma_{\mathrm{CRN}}^{m_3}$ is obtained by separating dark noise and fluctuating noise from the total noise,

$$\sigma_{\mathrm{CRN}}^{m_3} = \sqrt{(\sigma^{m_3})^2 - \left(\sigma_{\mathrm{dark}}^{m_3}\right)^2 - \left(\sigma_{\mathrm{fl}}^{m_3}\right)^2}, \tag{A1}$$

where $\sigma_{\mathrm{dark}}^{m_3}$ and $\sigma_{\mathrm{fl}}^{m_3}$ denote the STDs of dark noise and fluctuating noise in the third measurement, respectively.

On the other hand, the STDs of dark and fluctuating noise are consistent between the first and third measurements. This is because the dark noise is a constant for a specified SPD, and the fluctuating noise is solely determined by the backscattered photons reaching the SPD, which keeps the same level for the first and third measurements. This relationship is expressed as

$$\sigma_{\mathrm{dark}}^{m_3} = \sigma_{\mathrm{dark}}^{m_1}, \qquad \sigma_{\mathrm{fl}}^{m_3} = \sigma_{\mathrm{fl}}^{m_1}, \tag{A2}$$

where $\sigma_{\mathrm{dark}}^{m_1}$ and $\sigma_{\mathrm{fl}}^{m_1}$ are the STDs of dark noise and fluctuating noise in the first measurement, respectively.

Substituting Eq. (A2) into Eq. (A1), the STD of the CRN in the third measurement $\sigma_{\mathrm{CRN}}^{m_3}$ is rewritten as

$$\sigma_{\mathrm{CRN}}^{m_3} = \sqrt{(\sigma^{m_3})^2 - (\sigma_{\mathrm{dark}}^{m_1})^2 - (\sigma_{\mathrm{fl}}^{m_1})^2}. \tag{A3}$$

(2) Calculation of the STD of the CRN in the second measurement $\sigma_{\mathrm{CRN}}^{m_2}$

Beyond the effective nonlinear length, the impact of the nonlinear effect on the CRN is negligible, and CRN attenuation is determined by fiber loss. Thus, $\sigma_{\mathrm{CRN}}^{m_2}$ follows an exponential decay relationship:

$$\sigma_{\mathrm{CRN}}^{m_2} = \sigma_{\mathrm{CRN}_{51\,\mathrm{km}}}^{m_2} e^{-2\alpha z}, \tag{A4}$$

where $\sigma_{\mathrm{CRN}_{51\,\mathrm{km}}}^{m_2}$ is the STD of the CRN at the initial position (i.e., 51 km in this case) in the second measurement, and $\alpha = 0.19$ dB/km is the attenuation coefficient of the FUT.

Since the CRN evolution along the fiber is consistent for the second and third measurements, $\sigma_{\mathrm{CRN}_{51\,\mathrm{km}}}^{m_2}$ is calculated based on their overlapping region near 51 km, as expressed in Eq. (A5):

$$\sigma_{\mathrm{CRN}_{51\,\mathrm{km}}}^{m_2} = \sigma_{\mathrm{CRN}_{51\,\mathrm{km}}}^{m_3} \times 10^{19.3/10}, \tag{A5}$$

where $\sigma_{\mathrm{CRN}_{51\,\mathrm{km}}}^{m_3}$ is the STD of the CRN at the 51 km position in the third measurement, and $10^{19.3/10}$ accounts for the difference in backscattered photons reaching the SNSPD at 51 km between the second and third measurements. Substituting the data shown in Fig. 8(b) into Eq. (A3), we obtain $\sigma_{\mathrm{CRN}_{51\,\mathrm{km}}}^{m_3} = 4.8$. Substituting Eq. (A5) into Eq. (A4), the STD of the CRN in the second measurement $\sigma_{\mathrm{CRN}}^{m_2}$ is derived as

$$\sigma_{\mathrm{CRN}}^{m_2} = \sigma_{\mathrm{CRN}_{51\,\mathrm{km}}}^{m_3} \times 10^{19.3/10} e^{-2\alpha z} = 381 e^{-2\alpha z}. \tag{A6}$$

(3) Calculation of the noise STD of the second measurement σ^{m_2}

Combining the dark noise, the fluctuating noise, and the CRN, the STD of the total noise in the third measurement can be written as

$$\sigma^{m_2} = \sqrt{(\sigma_{\mathrm{dark}}^{m_2})^2 + (\sigma_{\mathrm{fl}}^{m_2})^2 + (\sigma_{R}^{m_2})^2}, \tag{A7}$$

where $\sigma_{\mathrm{dark}}^{m_2}$ and $\sigma_{\mathrm{fl}}^{m_2}$ are the STDs of dark noise and fluctuating noise in the third measurement, calculated using the same method as Eqs. (3) and (4), respectively. Figure 8(c) shows the experimental STD of the noises of the second measurement alongside the theoretical profiles predicted by Eqs. (A6) and (A7), with the total noise showing good agreement with the experimental results. This consistency validates the accuracy of the noise evolution analysis presented in this Appendix.

In conclusion, the noise evolution characteristics of the PC-OTDR system under the high intensity of the light pulse have been experimentally demonstrated and mathematically analyzed. The high intensity of light pulses suppresses the CRN through nonlinear effects, thereby enabling SNR improvement in long-range fiber sensing, as the experimental results show in Section 5.

APPENDIX B

In this appendix, the CRN is evaluated under different sampling bin widths t_{bin} with respect to the pulse width T. The derivation is based on the following assumptions and considerations of the CRN in the fiber.

(1) For simplicity, we considered Fourier-transform-limited Gaussian optical pulses. The coherence length L_c could be estimated by the temporal pulse width T according to $L_c = cT/n_{\mathrm{eff}}$, where c is the light velocity in a vacuum, and n_{eff} is the effective refractive index of the fiber.

(2) In the OTDR system, since the pulse and the backscattered light propagate in opposite directions, the backscattered lights from all the scattering points within the fiber segment with a length of $L_c/2$ are coherent. The phase differences of the backscattered lights from different combinations of scattering points in the fiber segment with a length of $L_c/2$ are totally random. Hence, they have the same contributions to the variations of the CRN.

(3) The transmission loss of the fiber is ignored in the derivation since the fiber segment considered in the derivation is quite short.

Considering the photon count in a specific time bin with a width of t_{bin}, it is the photon counting measurement result of the backscattering lights from all the scattering points within a short fiber segment with a length of L_{bin}, which is determined by t_{bin}, i.e., $L_{\mathrm{bin}} = ct_{\mathrm{bin}}/2n_{\mathrm{eff}}$. To analyze the CRN in this time bin, two cases should be considered, as shown in Fig. 9.

(1) $L_{\mathrm{bin}} \le L_c/2$, i.e., $t_{\mathrm{bin}} \le T$

As shown in Fig. 9(a), in this case, the backscattering lights of any two scattering points in the fiber segment are coherent, contributing to the CRN. The variation of the CRN in this time bin includes all these contributions. Hence,

$$\sigma_{\mathrm{CRN}}^2 \propto \int_0^{L_{\mathrm{bin}}} (L_{\mathrm{bin}} - z)\mathrm{d}z = \frac{L_{\mathrm{bin}}^2}{2} = \frac{c^2}{8n_{\mathrm{eff}}^2} t_{\mathrm{bin}}^2. \tag{B1}$$

(2) $L_{\mathrm{bin}} > L_c/2$, i.e., $t_{\mathrm{bin}} > T$.

This case is shown in Fig. 9(b). For the backscattering light from a scattering point at the location z, which is in the range of 0 to $L_{\mathrm{bin}} - L_c/2$, the backscattering lights from the scattering points in the range of z to $z + L_c/2$ are coherent with it and contribute to the CRN. On the other hand, for the backscattering light z, which is in the range of $L_{\mathrm{bin}} - L_c/2$ to L_{bin}, only the backscattering lights from the scattering points in the range

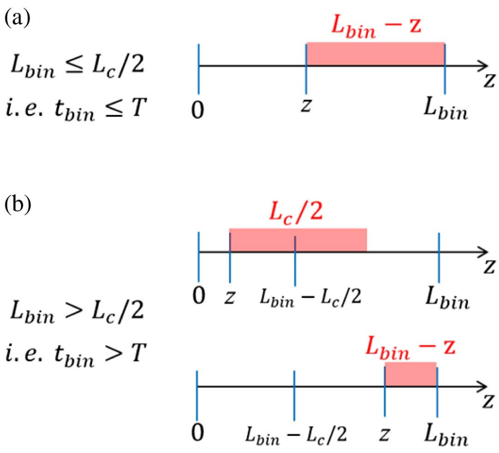

Fig. 9. Two cases in the analysis of the CRN. (a) $L_{\mathrm{bin}} \le L_c/2$ (i.e., $t_{\mathrm{bin}} \le T$) and (b) $L_{\mathrm{bin}} > L_c/2$ (i.e., $t_{\mathrm{bin}} > T$).

of z to L_{bin} are coherent with it and contribute to the CRN. Hence,

$$\begin{aligned}\sigma_{\mathrm{CRN}}^2 &\propto \int_0^{L_{\mathrm{bin}}-L_c/2} \frac{L_c}{2}\mathrm{d}z + \int_{L_{\mathrm{bin}}-L_c/2}^{L_{\mathrm{bin}}} (L_{\mathrm{bin}} - z)\mathrm{d}z \\ &= \frac{L_c L_{\mathrm{bin}}}{2} - \frac{L_c^2}{8} = \frac{c^2}{8n_{\mathrm{eff}}^2}(2Tt_{\mathrm{bin}} - T^2). \end{aligned} \tag{B2}$$

According to Eqs. (B1) and (B2), and considering the Rayleigh scattering count rate $R(z)$ and the measurement number N, the STD of CRN can be expressed as

$$\sigma_{\mathrm{CRN}} = \begin{cases} KR(z)t_{\mathrm{bin}}N & t_{\mathrm{bin}} \le T \\ KR(z)N\sqrt{2Tt_{\mathrm{bin}} - T^2} & t_{\mathrm{bin}} > T \end{cases}, \tag{B3}$$

where K is a scaling factor of this proportional relation, which relates to the characteristics of the light source and the FUT and can be estimated according to the experimental data.

Funding. Quantum Science and Technology-National Science and Technology Major Project (2024ZD0302502); Beijing Natural Science Foundation (4254076); National Natural Science Foundation of China (92365210); Tsinghua Initiative Scientific Research Program.

Disclosures. The authors declare no conflicts of interest.

Data Availability. Data underlying the results presented in this paper are not publicly available at this time but may be obtained from the authors upon reasonable request.

REFERENCES

1. A. H. Hartog, *An Introduction to Distributed Optical Fibre Sensors* (CRC Press, 2017).
2. B. Culshaw and A. Kersey, "Fiber-optic sensing: a historical perspective," J. Lightwave Technol. **26**, 1064–1078 (2008).
3. A. Usman, N. Zulkifli, M. R. Salim, *et al.*, "Optical link monitoring in fibre-to-the-x passive optical network (FTTx PON): a comprehensive survey," Opt. Switching Netw. **39**, 100596 (2020).
4. M. K. Barnoski, M. D. Rourke, S. M. Jensen, *et al.*, "Optical time domain reflectometer," Appl. Opt. **16**, 2375–2379 (1977).
5. X. Bao and Y. Wang, "Recent advancements in Rayleigh scattering-based distributed fiber sensors," Adv. Dev. Instrum. **2021**, 8696571 (2021).
6. J. Liu, Z. Lin, D. Liu, *et al.*, "High-dimensional quantum key distribution using energy-time entanglement over 242 km partially deployed fiber," Quantum Sci. Technol. **9**, 015003 (2024).
7. D. Liu, Z. Jin, J. Liu, *et al.*, "Chip-to-chip photonic quantum teleportation over optical fibers of 12.3 km," Light Sci. Appl. **14**, 243 (2025).
8. Z. Lin, Y. Gao, L. Zhou, *et al.*, "Integrated lithium niobate photonics for high-speed quantum key distribution," Opt. Quantum **3**, 195–200 (2025).
9. H.-S. Zhong, H. Wang, Y.-H. Deng, *et al.*, "Quantum computational advantage using photons," Science **370**, 1460–1463 (2020).
10. G.-L. Shentu, Q.-C. Sun, X. Jiang, *et al.*, "217 km long distance photon-counting optical time-domain reflectometry based on ultra-low noise up-conversion single photon detector," Opt. Express **21**, 24674–24679 (2013).
11. C. Schuck, W. H. P. Pernice, X. Ma, *et al.*, "Optical time domain reflectometry with low noise waveguide-coupled superconducting nanowire single-photon detectors," Appl. Phys. Lett. **102**, 191104 (2013).
12. Q. Zhao, L. Xia, C. Wan, *et al.*, "Long-haul and high-resolution optical time domain reflectometry using superconducting nanowire single-photon detectors," Sci. Rep. **5**, 10441 (2015).
13. B. Li, R. Zhang, Y. Wang, *et al.*, "Dispersion independent long-haul photon-counting optical time-domain reflectometry," Opt. Lett. **45**, 2640–2643 (2020).
14. M. Romanet, É. Rochat, J.-C. Beugnot, *et al.*, "Extended-range and faster photon-counting Brillouin optical time domain reflectometer," Optica **12**, 564–569 (2025).
15. Q. Zhao, J. Hu, X. Zhang, *et al.*, "Photon-counting optical time-domain reflectometry with superconducting nanowire single-photon detectors," in *IEEE 14th International Superconductive Electronics Conference (ISEC)* (IEEE, 2013), pp. 1–3.
16. J. Hu, Q. Zhao, X. Zhang, *et al.*, "Photon-counting optical time-domain reflectometry using a superconducting nanowire single-photon detector," J. Lightwave Technol. **30**, 2583–2588 (2012).
17. F. Calliari, M. M. Correia, G. P. Temporao, *et al.*, "Fast acquisition tunable high-resolution photon-counting OTDR," J. Lightwave Technol. **38**, 4572–4579 (2020).
18. M. Legré, R. Thew, H. Zbinden, *et al.*, "High resolution optical time domain reflectometer based on 1.55 μm up-conversion photon-counting module," Opt. Express **15**, 8237–8242 (2007).
19. B. Li, G. Deng, R. Zhang, *et al.*, "High dynamic range externally time-gated photon counting optical time-domain reflectometry," J. Lightwave Technol. **37**, 5899–5906 (2019).
20. L. E. Ynoquio Herrera, G. C. Amaral, and J. P. Von Der Weid, "Remote fiber Bragg grating-based sensor characterization with ultra-high-resolution tunable photon counting OTDR," in *SBMO/IEEE MTT-S International Microwave and Optoelectronics Conference (IMOC)* (IEEE, 2017), pp. 1–4.
21. G. P. Agrawal, *Nonlinear Fiber Optics*, 5th ed. (Academic Press, 2013).
22. P. Eraerds, M. Legre, J. Zhang, *et al.*, "Photon counting OTDR: advantages and limitations," J. Lightwave Technol. **28**, 952–964 (2010).
23. J. G. Proakis and D. Manolakis, *Digital Signal Processing* (Prentice Hall of India, 2006).
24. S. Das, M. G. Uddin, D. Li, *et al.*, "Nanoscale thickness octave-spanning coherent supercontinuum light generation," Light Sci. Appl. **14**, 41 (2025).
25. K. Shimizu, T. Horiguchi, and Y. Koyamada, "Characteristics and reduction of coherent fading noise in Rayleigh backscattering measurement for optical fibers and components," J. Lightwave Technol. **10**, 982–987 (1992).
26. Z. He, T. Kazama, Y. Koshikiya, *et al.*, "High-reflectivity-resolution coherent optical frequency domain reflectometry using optical frequency comb source and tunable delay line," Opt. Express **19**, B764–B769 (2011).
27. J. Zhou, Z. Pan, Q. Ye, *et al.*, "Characteristics and explanations of interference fading of a phi-OTDR with a multi-frequency source," J. Lightwave Technol. **31**, 2947–2954 (2013).
28. E. Diamanti, C. Langrock, M. M. Fejer, *et al.*, "1.5 μm photon-counting optical time-domain reflectometry with a single-photon detector based on upconversion in a PPLN waveguide," Opt. Lett. **31**, 727–729 (2006).
29. P. Healey, "Multichannel photon-counting backscatter measurements on monomode fibre," Electron. Lett. **17**, 751–752 (1981).
30. M. Wegmuller, F. Scholder, and N. Gisin, "Photon-counting OTDR for local birefringence and fault analysis in the metro environment," J. Lightwave Technol. **22**, 390 (2004).